

# Oxygen activated CVD growth of large-area multilayer h-BN on polycrystalline copper foils

Mohammad Wasil Malik<sup>a</sup>, Sami Ullah<sup>b</sup>, Bin Wang<sup>a,c</sup>, Sahar Jaddi<sup>d</sup>, Yun Zeng<sup>c</sup>, Jean-Pierre Raskin<sup>a,\*</sup>

<sup>a</sup> Institute of Information and Communication Technologies, Electronics and Applied Mathematics (ICTEAM), UCLouvain, Louvain-la-Neuve 1348, Belgium

<sup>b</sup> School of Physics, HH Wills Physics Laboratory Tyndall Avenue, Bristol BS8 1TL, United Kingdom

<sup>c</sup> School of Physics and Electronics, Hunan University, Changsha 410082, China

<sup>d</sup> Institute of Mechanics, Materials and Civil Engineering (IMMC), UCLouvain, Louvain-la-Neuve 1348, Belgium

## ARTICLE INFO

Communicated by: Joan M. Redwing

### Keywords:

G03: Nanomaterials and low dimensional structures

G04: Thin films and epitaxial growth

G08: Advanced growth technologies

T03: 2D materials

G04: Chemical vapor deposition

T03: Multilayer h-BN

## ABSTRACT

The synthesis of large-area multilayer hexagonal boron nitride (h-BN) is a prerequisite for advanced 2D material-based transparent electronics. The formation of large-area h-BN domains limits the possibility of grain boundary leakage current and mechanical ruptures of h-BN layers. In this work, we report the oxygen-activated synthesis of high-quality multilayer h-BN on polycrystalline copper foils, to reduce the nucleation site density and enhance the size of h-BN domains up to  $\sim 180 \mu\text{m}$ . The oxygen-activated synthesized h-BN domains are at least 20–30 times larger than the domains synthesized by the non-oxygen-based synthesis process.

Experimental results demonstrate that the h-BN domain size does not depend on the crystal orientation of the catalyst. X-ray photoelectron spectroscopy (XPS), Scanning electron microscopy (SEM), Atomic force microscopy (AFM), and Angle-resolved photoemission spectroscopy ( $\mu$ -ARPES) measurements together with Raman spectroscopy indicate that the synthesized h-BN layers are of high quality.

## 1. Introduction

The tremendous advancement in graphene technology has triggered researchers to explore and expand the 2D materials family. 2D hexagonal boron nitride has attracted researchers for its unconventional and enthralling properties: wide energy gap [1], atomically smooth surface [2,3], ultra-high transparency [5], and high flexibility [7]. Besides the electrical insulation, h-BN exhibits high thermal conductivity as well as adequate chemical and thermal stability.

These interesting properties make h-BN a distinctive material in several fields such as electronics [1,6], magnetism [14], photonics [1,11], optoelectronics [4,12], and electromechanical applications [13]. The  $sp^2$  hybridized boron and nitrogen atoms are arranged in a hexagonal honeycomb structure [9] that provides ultra-high mechanical strength [8] in the basal plane direction. h-BN shows a sharp absorption in the deep ultraviolet (DUV) range [10] when it is reduced to a monolayer from its bulk counterpart. Defects in the crystalline structure of h-BN are highly bright photon emitters [14]. Moreover, h-BN is also a direct wide bandgap semiconductor with a strong UV emission [15,16].

h-BN has been considered as a promising atomically smooth insulating substrate for a range of 2D materials. Being an isomorph of graphene with a lattice mismatch of less than 1.6 %, h-BN is an ideal substrate for the epitaxial growth of graphene [38]. The above-mentioned extensive range of applications require high quality and a large area of h-BN layers. Mechanically exfoliated h-BN layers are of high quality but provide small flakes isolated and randomly distributed while large or even continuous areas of h-BN are composed of smaller individual domains that can be chemically synthesized. Higher nucleation site density results in smaller grain size that ultimately leads to a remarkable increase in the grain boundaries known as h-BN defects [14,36]. These defects give rise to charge puddles and surface roughness that result in poor device performance [2]. Therefore, defects or control of grain boundaries in h-BN layers are essential for excellent physical properties and higher device efficiency. Attempts have been made in recent years to produce high quality and large area h-BN via chemical vapor deposition (CVD) [17–27], plasma-enhanced atomic layer deposition [28], metal-organic chemical vapor deposition [29], molecular beam epitaxy [30–32] and liquid phase exfoliation processes [33–35]. However, for

\* Corresponding author.

E-mail address: [jean-pierre.raskin@uclouvain.be](mailto:jean-pierre.raskin@uclouvain.be) (J.-P. Raskin).

<https://doi.org/10.1016/j.jcrysgro.2023.127088>

Received 12 October 2022; Received in revised form 5 January 2023; Accepted 9 January 2023

Available online 13 January 2023

0022-0248/© 2023 Elsevier B.V. All rights reserved.

the large growth of single-crystalline h-BN, chemical vapor deposition is preferred over the other above-mentioned processes. In addition, the CVD process is widely adapted for the synthesis of 2D materials due to its low cost and simpler design. The copper substrate [10,18,22,23,25,36] is currently the most used catalyst for the growth of graphene and h-BN. A wide range of other catalytic substrates have been already utilized such as Fe [21], Ag [37], Pt [43], Ni [27] to get better control over the synthesis and other non-catalytic substrates like Si [47], and Ge [52] to avoid the tedious transfer process. Different precursors have been proposed and tested to achieve excellent growth conditions. The widespread precursors for the h-BN CVD growth are ammonia borane ( $\text{BH}_3\text{-NH}_3$ ) [10,18,22,25], B-trichloroborazine ( $\text{B}_3\text{N}_3\text{H}_3\text{Cl}_3$ ) [48], and borazine ( $\text{B}_3\text{N}_3\text{H}_6$ ) [17,21]. All aforementioned precursors have the advantage of having 1:1 boron to nitrogen stoichiometry. On the other hand, heterogeneous pyrolysis of  $\text{B}_2\text{H}_6$  [45],  $\text{BCl}_3$  [46],  $\text{BF}_3$  [47] together with  $\text{NH}_3$  has also been reported.

Recently, researchers have highlighted the interest in trimethylamine borane ( $\text{CH}_3)_3\text{N.BH}_3$  as h-BN growth precursor [49]. Despite all of these efforts, the size of the h-BN domains is still much smaller than the graphene domains synthesized by the CVD process on a metallic substrate. This is ascribed to the immense difference of adsorption energies between carbon atoms and the B-N pairs on the Cu surface based on first-principle calculations [19,23]. Unlike carbon, boron and nitrogen atoms show different solubility rates [24] within the substrate (Cu, Ni, Fe, etc.) at a high temperature which leads to inhomogeneous and uncontrolled growth of h-BN. It may alter the boron to nitrogen ratio, which then results in poor quality and possibly modified properties. Researchers have reported the typical size of h-BN domains in the order of a few micrometers in most of the published articles [21]. Since the early development of h-BN growth, several investigations have been carried out to control the nucleation site density.

Roland *et al.* proposed electrochemical polishing to smoothen the Cu surface, and thus prevent unwanted nucleation occurring at the rough and defected copper surface [25]. Metallic thin films including Ni [17], Co [19], Fe [24], Au [38], Cu [41], and Rh [39,40] deposited on the ultra-smooth surface of Si, quartz, and sapphire have been reported in the literature to achieve high-quality large area h-BN. Table S1 summarizes different large area processes previously mentioned in the literature. Lu *et al.* utilized Cu-Ni alloy to enlarge the size of the domains [20]. Wang *et al.* demonstrated an enormously large triangular domain up to 330  $\mu\text{m}$  on the liquid copper surface by using water vapor during the growth of h-BN [42]. The liquid metallic surface provides a smooth and grain boundary-free substrate. This further requires a higher temperature ( $>1087^\circ\text{C}$ ) which is also responsible for the quality growth and large area synthesis [26]. Metal pockets formation also improves the nucleation site densities by minimizing the partial pressure of the precursor which is quite an important parameter to avoid the pre- and post-growth or secondary nucleation [27,44]. Some other strategies including annealing of the metallic substrate [59], precursor feeding rate [18], catalytic substrate orientation [52,53], and controlling of the carrier gas are crucial to grow a large area of h-BN.

The above-mentioned synthesis processes require specific pre- or in situ processing such as polishing, pre-oxidation in air, or implementation of foreign materials, which are not very common and cumbersome to customize the instruments in such a way to obtain similar results. Earlier, it has been demonstrated that in the presence of oxygen, graphene nuclei are reduced and trigger large area AB stacked bilayer graphene [60,61]. In the case of h-BN CVD growth, the role of oxygen has been rarely investigated. It has been noted that the introduction of oxygen for CVD h-BN growth not only decreases the energy barrier for precursor dehydrogenation but also improves the nucleation site densities [54]. Chang *et al.* have demonstrated that oxide-assisted h-BN synthesis improves the h-BN domain size [36]. They have concluded that a pre-oxidized mechanically polished surface is crucial for large area h-BN domains. They were able to achieve the single layer h-BN grain of 20  $\mu\text{m}$  by ambient pressure chemical vapor deposition (APCVD).

Babenko *et al.* have demonstrated a novel approach by oxidizing a carburized iron foil at low temperatures [63]. By this integrated approach, they were able to manage single layer h-BN up to 1.1 mm and bilayer h-BN up to 180  $\mu\text{m}$ . Lin *et al.* have also presented a similar effect for their multilayer h-BN growth [51]. They maintained a small partial pressure of the air around 20 mTorr in the CVD chamber to grow multilayer h-BN. In their case, no individual domain has been observed. Besides, the previously reported processes have precisely considered the large area growth for the single layer h-BN only. This atomically thin boron nitride offers very low tunneling resistance and thus is not suitable for the gate dielectric layer in field-effect transistors (FETs) [62]. Therefore, a large-area synthesis of multilayer h-BN is of great importance.

In this work, a low-pressure chemical vapor deposition (LPCVD) process for the synthesis of crystalline multilayer h-BN is performed. Here, the effect of oxygen-based annealing on the copper foils is investigated to achieve large area h-BN growth. The copper substrate was oxidized by oxygenated argon for few hours to eliminate possible organic impurities and formed a protective oxide layer prior to the growth. This oxygen-activated chemical vapor deposition (OA-CVD) exhibits an enormous increase in multilayer h-BN domain size. We have compared our OA-CVD growth results with the hydrogen annealed CVD (HA-CVD) growth. The OA-CVD and HA-CVD take place under two different pressure regimes on copper foils without any surface pretreatment. OA-CVD synthesized h-BN domains having a thickness of 2–4 nm exhibit multi-shape domains all over the substrate while the HA-CVD synthesized h-BN domains emerge out as triangular-shaped predominantly which has been attributed to an interplay between the active precursor concentration i.e. ratio of B and N, the substrate temperature [23], substrate type (whether polished or unpolished) [25] and the presence of oxidised species on the surface of Cu which is more relevant in our case as will be discussed later [67]. The domain size of the crystals synthesized by OA-CVD process is 20–30 times larger than the HACVD ones. The size and thickness of as grown multilayer h-BN are characterized by optical microscopy, scanning electron microscopy (SEM) and atomic force microscopy (AFM). The quality of h-BN layers is evaluated by x-ray photoelectron spectroscopy (XPS), angle-resolved spectroscopy ( $\mu$ -ARPES), photoemission electron microscopy (PEEM), and raman spectroscopy.

## 2. Experimental details

### 2.1. h-BN synthesis

Thin films of h-BN are prepared by a novel OA-CVD process at low pressure. The 50  $\mu\text{m}$ -thick copper foil was purchased from Advanced Materials. The copper foil is loaded into the CVD chamber without any pretreatment or cleaning. After loading the copper substrate, a few mg (20–30 mg) of ammonia borane is separately loaded in a quartz boat into a separate anti-chamber, which is wrapped with a highly resistive silicone belt. CVD equipment quickly pumps down at low pressure to remove all air contaminations. After that, the system is purged with a heavy flow of 99.99 % pure argon at a rate of 556 sccm for at least 5 min to remove all the contaminants from the chamber. Then, the system heats up to 800–900  $^\circ\text{C}$  for the pre-oxidation of copper foil with a controlled flow of 556 sccm Ar and 3–6 sccm of  $\text{Ar/O}_2$  (500 ppm). The sample oxidizes at near ambient pressure for 30–120 min. Before starting the growth, 7 sccm hydrogen (10 % in Ar) is purged into the chamber and the temperature is ramped up to 1060  $^\circ\text{C}$  to initiate the growth. In the meantime, the heating of the anti-chamber, and the temperature are maintained just below the decomposition temperature of ammonia borane. Just before the growth, the pressure of the CVD chamber is reduced to 200–400 mbar and the temperature of the anti-chamber is increased to  $94 \pm 2^\circ\text{C}$ . The growth takes place at a temperature of 1060  $^\circ\text{C}$  for 45 to 60 min. During the growth duration, the flow of  $\text{Ar/H}_2$  is kept around 51–85 sccm while the flow of Ar is kept

around 0–35 sccm. After that, the heating of the ammonia borane chamber is stopped and the argon flow rate is set to zero. The CVD chamber is quickly cooled down to stop the secondary growth/amorphous BN species on the crystalline h-BN in the presence of continuous flow of Ar/H<sub>2</sub>.

## 2.2. Transfer of h-BN

After the growth, h-BN synthesized copper foil is mounted on a flat silicon substrate with the help of Kapton tape. Then, the h-BN films were coated with a film of 4 % polymethylmethacrylate (PMMA) at 3000 rpm for 1 min, and the sample is left to dry overnight. The copper substrate was then etched in an aqueous FeCl<sub>3</sub> solution and the PMMA/h-BN stack successively rinsed 5–8 times in a DI water bath. The stack is placed on a 300 nm oxidized silicon substrate. The sample was left at room temperature to dry overnight. A layer of fresh PMMA is applied to the transferred stack to soften the old PMMA layer. After a few minutes, the transferred h-BN on SiO<sub>2</sub> substrate was left into hot acetone for 20–30 min to etch away the PMMA layer.

## 2.3. XPS

The XPS analysis is carried out with an SSX 100/206 photoelectron spectrometer from Surface Science Instruments (USA) equipped with a monochromatized micro-focused Al X-ray source (powered at 20 mA and 10 kV). The samples were fixed with double-sided tape onto a ceramic carousel. The pressure in the analysis chamber was around 10<sup>-6</sup> Pa. The angle between the surface normal and the axis of the analyzer lens was 55°. The analyzed area was approximately 1.4 mm<sup>2</sup> and the pass energy was set at 150 eV. Under these conditions, the full width measured at half maximum (FWHM) of the Au 4f 7/2 peak for a clean gold standard sample was about 1.6 eV. A flood gun set at 8 eV and a Ni grid placed 3 mm above the sample surface were used for charge stabilization. The following sequence of spectra was recorded: survey spectrum, C 1s, O 1s, N 1s, B 1s, Cu 2p, and C 1s again to check the stability of charge compensation with time. The C-(C, H) component of the C 1s peak of carbon has been fixed to 284.8 eV to set the binding energy scale. Data treatment was performed with the CasaXPS program (Casa Software Ltd, UK), some spectra were decomposed with the least-squares fitting routine provided by the software with a Gaussian/Lorentzian (85/15) product function and after subtraction of a non-linear baseline. Molar fractions were calculated using peak areas normalized based on acquisition parameters and sensitivity factors provided by the manufacturer.

## 2.4. TOF-SIMS

SIMS depth profiles are made using a TOF.SIMS5 (IONTOF GmbH, Münster, Germany) time-of-flight secondary ion mass spectrometer. The instrument is equipped with a Cs + gun as the sputtering source and a liquid metal ion gun (Bi) as an analytical source both mounted at 45° concerning the sample surface. The time-of-flight mass analyzer is perpendicular to the sample surface. Depth profiling is carried out in the ‘interlaced’ mode. The Cs + ion source was operated at 1 keV with a d.c. current of 10nA. For depth profiling, the focussed Cs beam of primary ions was rastered over an area of typically 600 × 600 μm<sup>2</sup>. A pulsed beam of 30 keV Bi<sup>5+</sup> (a.c. current of 0.1 pA) ions is employed to provide mass spectra from a 200 × 200 μm<sup>2</sup> area in the center of the sputter crater. No charge compensation was necessary on these conductive samples. All data analysis is carried out using the software supplied by the instrument manufacturer, SurfaceLab (version 6.8).

## 2.5. PEEM and μ-ARPES

The surface analysis of samples was performed at Bristol NanoESCA Facility in ultrahigh vacuum (UHV) chambers. The samples underwent

many annealing procedures for cleaning purposes. Work function mapping and full-wave vector ARPES were obtained at a low temperature of 34 K (liquid He) with NanoESCA II energy-filtered PEEM (EF-PEEM) using a non-monochromatic Hg source (hν ≈ 5.2 eV) for WF mapping and a monochromated helium (hν = 21.2 eV) source for ARPES.

## 2.6. Raman spectroscopy

LabRAM HR is an instrument from Horiba Scientific, which combines a very high spectral and spatial resolution with the ability to probe samples with three different laser wavelengths: 488 nm, 514 nm, and 633 nm. The different available gratings allow sweepings of the sample from 80 cm<sup>-1</sup> to 3500 cm<sup>-1</sup> in a single acquisition. A motorized stage allows XY and Z mapping of defined areas to investigate point-by-point characteristics of a determined area in the sample. All the Raman analysis is carried out using green laser with an acquisition time of 600 s. The Raman map is plotted by taking 546 points in the non-sweeping mode. To calculate the statistical measurement of the peak location and the FWHM a sample size of 98 and 22 random locations is considered respectively.

## 2.7. SEM and optical microscopy

Zeiss Axio Imager Vario A2 Research microscope with a wide range of incident light techniques (BF, DF, DIC, TIC) and equipped with a CCD camera having a sample holder: up to 8" and can go up to 100× magnification is used. The h-BN domain shape, size, and density were observed by scanning electron microscopy FIB-SEM, Zeiss Auriga series equipped with unique GEMINI detector.

## 2.8. AFM

AFM images are recorded by Bruker icon dimension multimode scanning probe microscopy. The h-BN samples were transferred to 300 nm SiO<sub>2</sub>/Si substrate before the imaging.

## 2.9. XRD

XRD measurements are performed using a Bruker D8 advanced, equipped with a linkeye XE-T detector and Cu source. The two-theta range from 5 to 60° is scanned with an increment of 0.015° and an integration time of 0.15 s using a Bragg Brentano geometry. The Bruker software EVA is used for data processing by using either the COD or PDF 2 database for phase recognition.

## 3. Results and discussion

In this work, copper foils (Cu) are used as the catalytic substrate for h-BN growth. Fig. 1(a) shows a schematic representation of the experimental setup. The synthesis of h-BN takes place in a CVD oven composed of a 4-inch quartz tube with digital mass flow controllers. Ammonia borane powder (BH<sub>3</sub>NH<sub>3</sub>) is supplied as the precursor and placed into an aluminum anti-chamber wrapped with a highly resistive silicone rubber heating tape. Here, we use two separate heating systems to provide better control over the synthesis process. The CVD system has been customized in a way that the vapor of ammonia borane (AB) vapors go into the synthesis chamber during the growth duration only. The heating of AB takes place in two different segments (pre- and post-heating) [see supplementary information, Fig. S1 (a)] to avoid any possibility of pre-nucleation of h-BN. During the pre-heating, we supply the thermal energy to maintain the temperature well below the decomposition temperature of the AB (<70 °C) [55]. Later on, during the post-heating [Fig. S1 (a)], the temperature is maintained at around 95 ± 3 °C. The h-BN growth triggers when the temperature goes above 70 °C. The carrier gas (Ar) delivers the AB vapor with mainstream gas into the

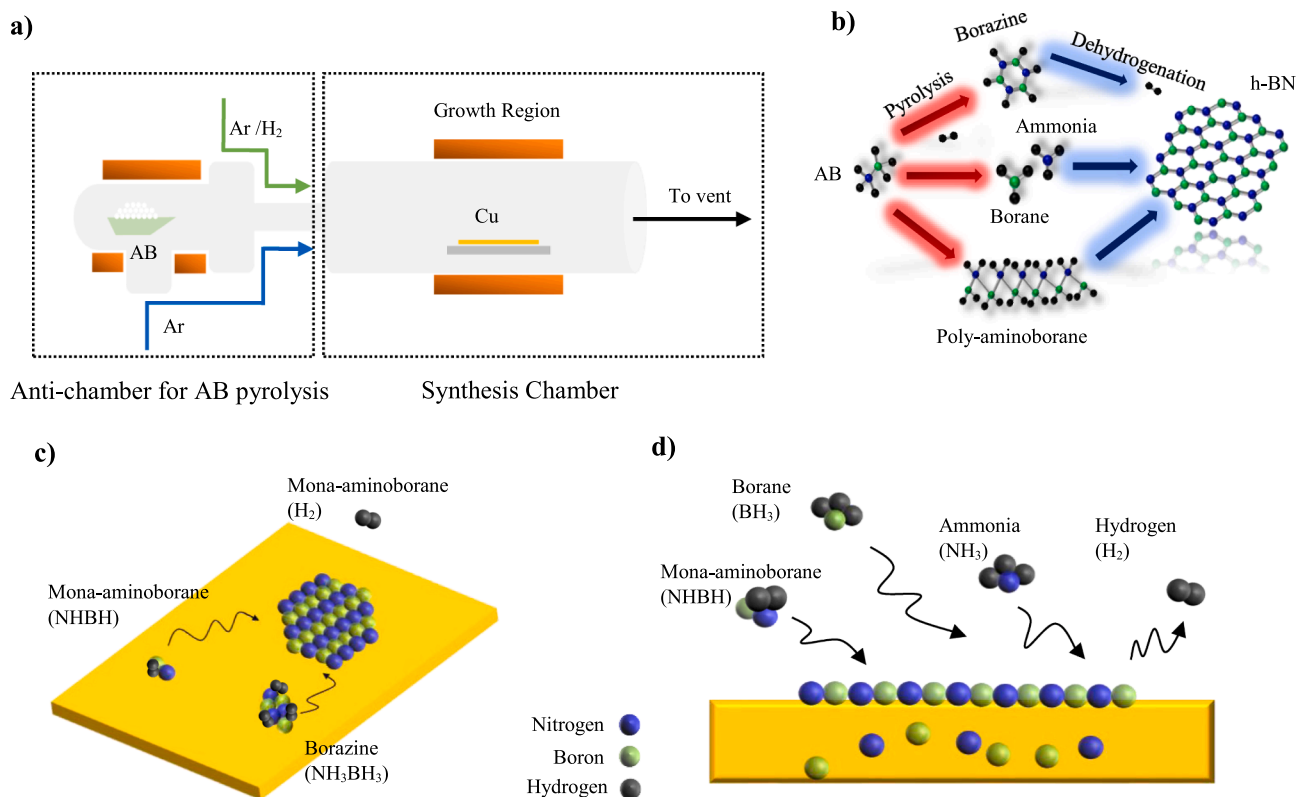


**Fig. 1.** Schematic representation of the CVD process. (a) 2D representation of the CVD chamber having a separate antichamber for AB decomposition, AB vapors delivered into synthesis chamber by Ar and Ar/H<sub>2</sub>. (b) Schematic diagram of pyrolysis showing molecular development from AB dissociation. (c) Schematic representation of surface-mediated h-BN growth mechanism on copper foils. (d) Schematic diagram of segregation/quenching mechanism of h-BN growth.

synthesis chamber where a copper substrate is kept at 1060 °C on a quartz support wafer. Our CVD process shows multilayer h-BN growth on the copper substrate. AB decomposition takes place in the temperature range of 70–95 °C that results in different gaseous species such as borane (BH<sub>3</sub>), ammonia (NH<sub>3</sub>), diborane (B<sub>2</sub>H<sub>6</sub>), monoamino borane (NHBH), borazine (B<sub>3</sub>N<sub>3</sub>H<sub>6</sub>), hydrogen (H<sub>2</sub>), and other complex species [50]. A schematic representation of AB dissociation is illustrated in Fig. 1(b). Thermogravimetric analysis (TGA) analysis has been carried out to confirm the hydrogen evolution process from AB [see Fig. S1 (b)]. AB evolves the hydrogen gas when decomposing to active BN species. The decomposition of AB is explained in detail by the chemical equations illustrated in Table S2 (I). These gaseous species are carried by argon and hydrogen into the synthesis chamber and get adsorbed on the copper surface. Active species such as mono-amino borane, borazine dehydrogenate and generate stable nuclei for h-BN growth. The other active species dehydrogenate and attach to the stable nuclei resulting in the size increment of the h-BN domains that finally coalesce into the continuous layer by the constant supply of active species. Fig. 1(c) and 1(d) show the schematic representation of the h-BN growth mechanisms that are (i) surface-mediated growth widely accepted for the CVD-grown 2D materials, and (ii) the segregation/quenching of boron and nitrogen atoms during the cooling of CVD furnace, respectively. Epitaxial growth of monolayer h-BN takes place on the surface while the boron and nitrogen diffuse into the copper substrate at high temperature, which precipitates out during the cooling process and nucleates further layers of h-BN as demonstrated in Fig. 1(d). Takesaki *et al.* have demonstrated a similar concept for bilayer graphene synthesis on Cu-Ni alloys [58]. Chang and coworkers have also illustrated the epitaxial growth of monolayer h-BN [36]. The depth profiling of copper foils after the growth further confirms that the segregation of boron takes place during the cooling process. Fig. S2 demonstrates the presence of metallic boron inside the copper substrate. Fig. S3 (a) illustrates the synthesis protocol

for the non-oxygen-based CVD, i.e. hydrogen annealed CVD (HA-CVD) process. In the HA-CVD process, the copper surface is annealed in Ar/H<sub>2</sub> at near ambient pressure. A plethora of organic impurities remain on the substrate due to the lack of oxidative agents and offer additional nucleation sites for the h-BN synthesis leading to smaller h-BN domains [Fig. 2(a–b)]. On the other hand, in the oxygen-activated CVD (OA-CVD) process, we introduce a pre-oxidation step that actively oxidizes potential organic impurities and passivates the copper surface by a thin oxide layer. The synthesis protocol of the OA-CVD process is illustrated in Fig. S3 (b). In the presence of copper oxide, the catalytic property of copper extinguishes and BN molecules require higher dissociating energy to initiate the growth. This concept was adapted by Chang *et al.* for the single-layer h-BN growth pre-oxidized mechanically polished copper foils [36]. The oxidation of copper foils in the air creates an oxide barrier on the surface to prevent uncontrolled nucleation. However, due to direct exposure of the oxide layer to the mainstream gas (Ar/H<sub>2</sub>), the copper oxide quickly reduces and offers a fresh catalytic Cu surface for growth after only a couple of minutes. Consequently, it results in pretty small h-BN domains. Although, they sufficiently managed to attain a maximum domain size of about 20 μm. On the contrary, in our OA-CVD process, the oxidation takes place by 500 ppm of oxygen altogether with argon during the pre-oxidation step [Fig. S3 (b)] which was absent in the HA-CVD process. This reduction of nucleation site density due to oxidizing the Cu surface has been discussed earlier in the case of graphene [72–74]. The oxidation in the CVD chamber itself provides better control over the thickness of the oxide layer by regulating the flow rate of oxygen as compared with the uncontrolled oxidation of copper foils in the air. Most of the organic species are oxidized by the introduction of oxygen at a high temperature around 800–900 °C [see Table S2 (II)] due to the surface confinement as presented in [68–70]. The non-confined copper surface which is directly exposed to the mainstream gases heavily oxidizes typically in 1–2 hours of duration while the bottom

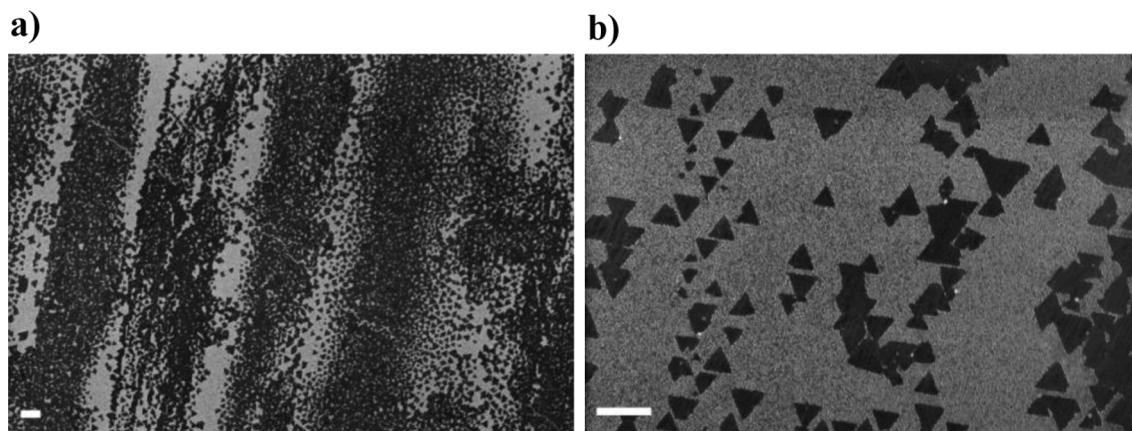


**Fig. 2.** SEM images of HA-CVD synthesized h-BN domains. (a–b) SEM images of HA-CVD synthesized h-BN domains on copper foils. The scale bar is 2  $\mu\text{m}$  and 1  $\mu\text{m}$  for images a & b, respectively.

surface-confined by quartz support forms a gradient of a thin copper oxide layer as depicted in the schematic diagram of Fig. 3, [see also Fig. S4 (a–b) for the experimental pictures of copper foils]. The oxide layer confined by the quartz support lasts longer than the non-confined thick copper oxide [Fig. S4 (cvd)]. This substrate confinement effect keeps very low partial pressure of hydrogen during the ramping period, which results in slower etching of copper oxide and helps to maintain the oxide layer during the growth regime as well. Moreover, the copper confinement also maintains the low partial pressure of AB vapor that favors the growth of large-area h-BN domains. The h-BN domains formed on this confined surface are in the range of 10–180  $\mu\text{m}$  [Fig. S15 (a)] when the oxidation time varies from 30 to 120 min [Fig. 4(a–c)]. Further oxidation of copper foils does not improve the size of the domains certainly due to the saturated copper oxide formation. As illustrated in Fig. S3 (a) and S3 (b), the HA-CVD growth was followed by a one-hour hydrogen treatment (annealing) of the copper substrate at 1060  $^{\circ}\text{C}$  whilst in the OA-CVD synthesis protocol, this treatment was replaced by oxygenated argon for 1–2 hours of oxidation in a temperature range of 800–900  $^{\circ}\text{C}$  and then the temperature is raised to 1060  $^{\circ}\text{C}$

in the presence of argon and hydrogen. The key difference between both processes is the pre-oxidation step, which takes place before the growth at least for 30 min to create the thin oxide layer on the copper surface. The introduction of hydrogen after the oxidation of copper foils is to prevent the surface deterioration of the substrate [71,72], which occurs due to the trapped surface oxygen when the copper oxide is exposed to the active BN species. The surface deterioration also can be seen when the copper substrate is oxidized at a high temperature or with a heavy concentration of oxygen. This deterioration is usually formed as grooves and holes that create roughness/irregularities all over the surface Fig. S5 (a–c). Sometimes it also leaves black burn spots on h-BN layers. The h-BN domains produced by the OA-CVD process are at least 20–30 times larger than the domains synthesized by the HA-CVD process as shown in Fig. 2(b) and Fig. 4(a–c). The pre-oxidation step duration influences the size of the domains when it is increased from 30 min to 2 hours and it is attributed to the thin  $\text{CuO}_x$  layer and the surface confinement effect. The natural confinement of copper foil provided by the quartz support enables us to achieve highly reproducible growth [Fig. S5 (d–e)]. Typically, our process growth is carried out for 30–45 min to achieve

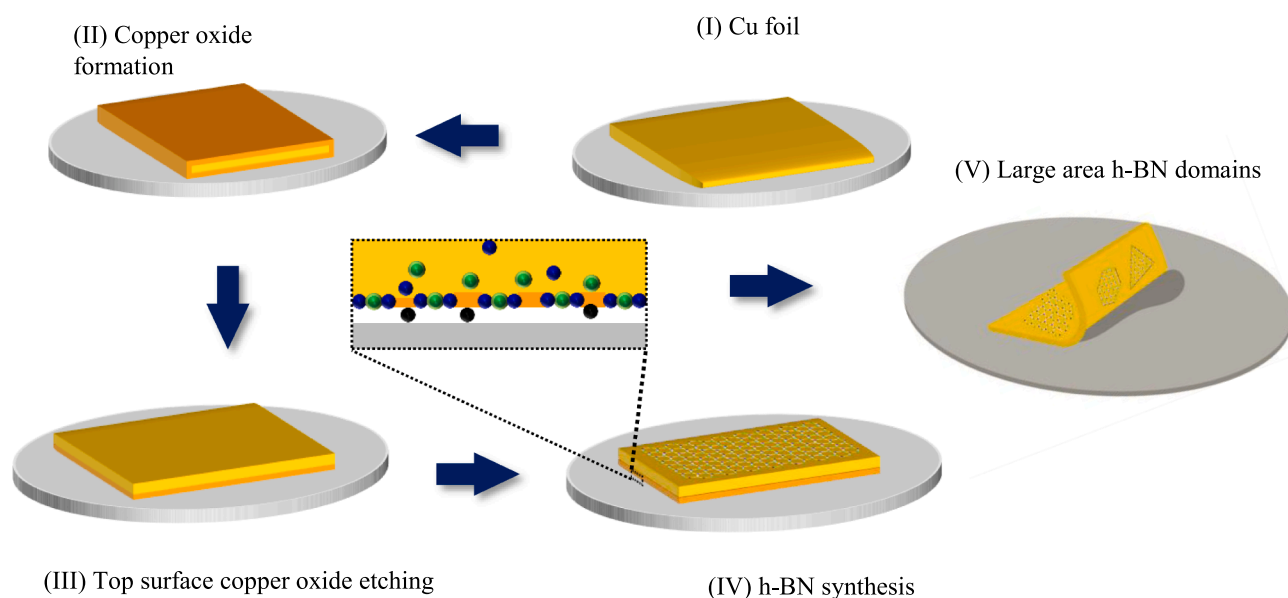


**Fig. 3.** Schematic illustration of OA-CVD synthesized h-BN. The synthesis of h-BN takes place in four different stages. (I) The first stage demonstrates placing the purchased copper foils in the CVD chamber and ramping-up to oxidation temperature. (II) In this stage the oxidation of copper foil takes place all around which is the key feature of large-area synthesis of h-BN. (III) In this stage the copper oxide is partially reduced by the insertion of a small amount of Ar/H<sub>2</sub>. This is the part where CVD ramps-up to growth temperature. (IV) This is the final stage of growth in which AB precursor is supplied to the chamber and h-BN growth takes place on both surfaces of copper foils. (V) The large h-BN domains found on the confined surface as shown in the schematic representation.

## Low Temperature Copper Oxidation (850 °C)

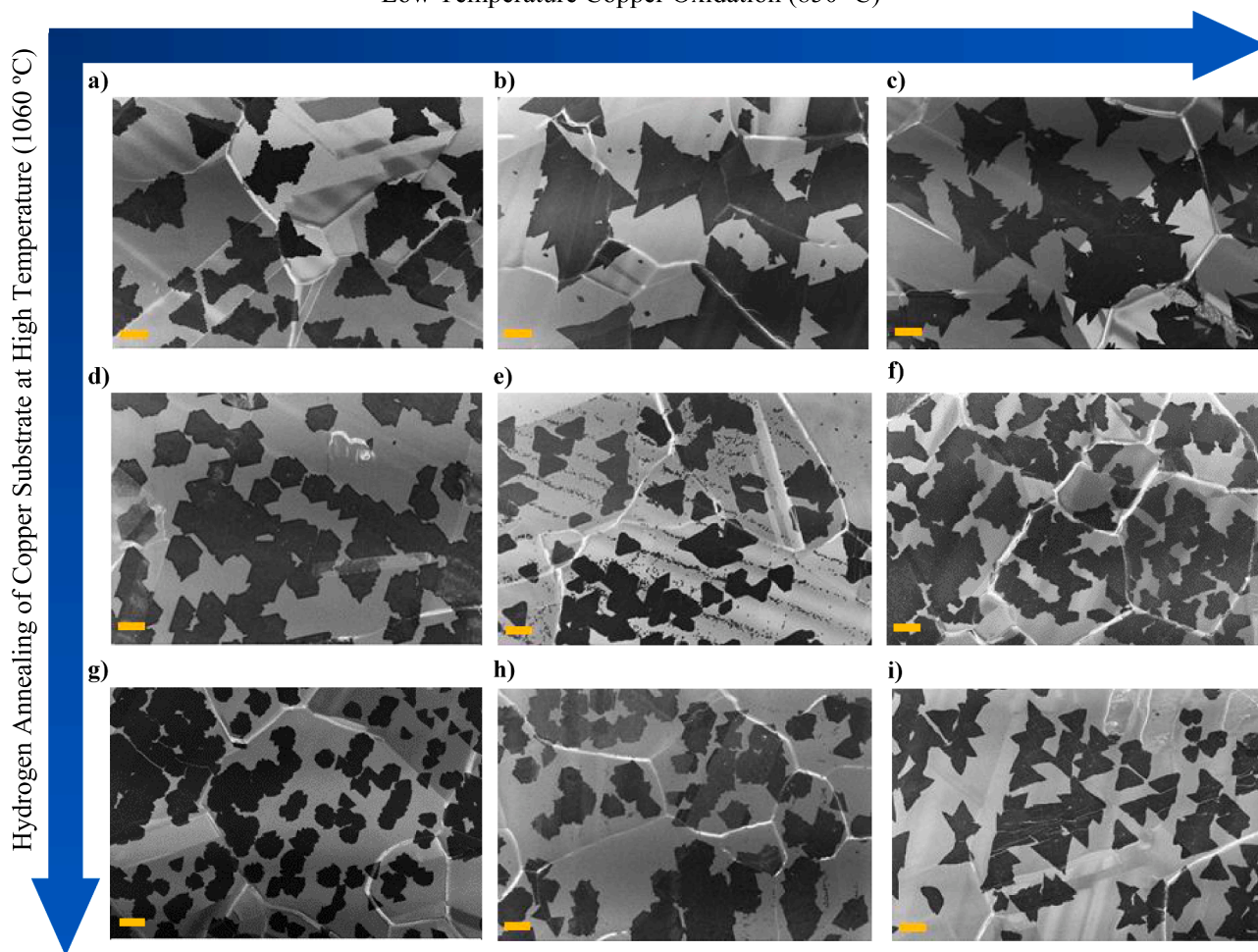


**Fig. 4.** SEM images panel of OA-CVD synthesized h-BN domains on copper foils. (a–i) h-BN domains on 30, 60, and 120 min oxidized copper foils respectively, with different hydrogen annealing periods of; (a–c) 0 min. (d–f) 30 min. (g–i) 60 min.

distinguished h-BN domains while elongated growth duration up to 60 min or more produces continuous layers [Fig. S6 (a–d)]. The control over the continuous layer formation not only depends on the longer growth duration but also can be achieved by maintaining the flow rate of the hydrogen and the argon which has been used as carrier gases in our processes. A higher flow rate increases the precursor partial pressure in the CVD chamber during the growth and leads to the complete merging of the h-BN domains in a shorter span of time. However, this can be achieved by only increasing the flow rate of hydrogen but here we are also using a little flow of argon to push the precursor into mainstream gas, which can be easily comprehended by the schematic diagram of the CVD setup illustrated in Fig. 1(a). The continuous h-BN formation via different combinations of hydrogen and argon flow rates has been illustrated in Fig. S7 (a–i). In our process, h-BN grows on both surfaces; the non-confined surface offers very high nucleation site density and formed a continuous layer in few minutes. No individual distinct domains have ever been observed on the non-confined copper surface. In addition, we also have studied systematically the effect of different gases that purged during the pre-oxidation step such as Ar, and N<sub>2</sub>, other than H<sub>2</sub> and Ar + Ar/O<sub>2</sub>. Comparative results are shown in Fig. S8 (a–d). The HA-CVD synthesis results in very small domains having an average size of 1–5 μm only. In the presence of Ar and N<sub>2</sub>, we observe a drastic change in the shape and the size of domains as compared with the HA-CVD process. We think the shape variation is due to the variation in the precursor concentration and/or the substrate temperature that results into the stoichiometry modification induced due to H, N, B, C, O being

absorbed and released by the Cu in different proportions at different moment of the process, supported by the earlier studies where symmetric hexagonal h-BN crystals were grown, isotropically, at higher precursor concentrations and higher heating temperature while at lower precursor concentration triangular shapes were formed due to anisotropic growth [67]. Meanwhile the transformation from hexagonal crystals into triangular crystals of h-BN has also been found to occur when the precursor heating temperature is changed that results into decreased precursor flow concentration. In our case HA-CVD growth has resulted into the triangular shape while OA-CVD into the hexagonal crystals which has been attributed to the increased oxidation (on the Cu surface) or the presence of oxidised species that facilitate precursor dissociation at lower energy. This results into lower energy barrier for h-BN growth where BN radicals further bond to both N and B-terminating edges and hence different shapes evolve. Ar annealed CVD (AA-CVD) process leads to a domain average size of ~10–15 μm almost similar to the results obtained in the presence of the N<sub>2</sub> annealed CVD (N-CVD) process except for the shape of domains. The comparison of respective CVD synthesis protocols is illustrated in Fig. S9 (a–d). We think that the change in the size of h-BN domains occurs by the elimination of residual organic impurities of copper foils by a thin oxide passivation layer formed by the residual oxygen and humidity present in the argon and nitrogen feedstock. To further confirm the role of the thin oxide layer, we have carried out some experiments with a longer annealing duration in the presence of hydrogen followed by the pre-oxidation step [Fig. S10 (a)]. The longer annealing in hydrogen further decreases the size of the

h-BN domains. We believe that longer annealing in the presence of hydrogen eliminates the passivated copper oxide layer and during the growth B-N radicals directly nucleate on the copper surface. The increase in the size may be attributed only to the surface confinement effect on a clean copper surface [Fig. 4(a–i)]. Our CVD process results into miscellaneous shapes of h-BN domains attributed to the surface oxygen and copper vapor effect caused by the surface confinement effect. Indeed, in the OA-CVD process, heat treatment of the copper substrate is almost double than HA-CVD process, which may introduce the doubt about the role of monocrystalline copper grains caused by the oxidation and long hightemperature heat treatment as shown by Wu *et al.* They have successfully demonstrated that pre-oxidized copper foils in the air turned into a range of single-crystalline copper substrate after long annealing of copper foils in the presence of hydrogen [56]. To eliminate the doubt we have performed the XRD analysis on the samples prepared by the HA-CVD, AA-CVD, NCV, and OA-CVD process under similar conditions without introducing the precursor. In comparing the results, we find that the smallest domains prepared by the HA-CVD process and the largest domains prepared by the OA-CVD belong to the same family of copper orientation, see Fig. 5(a). The major fraction of copper crystallinity belongs to the Cu (200), Cu (111), and Cu (220). It confirms the fact that large area h-BN synthesis does not depend on any specific orientation of the underlying copper substrate. Although, the non-homogeneity and seamless merging of the synthesized h-BN domains depends on the copper surface orientation. The optical microscopy images show that a few copper grains have seamless merging while the other grains have inhomogeneity and visible grain boundaries [Fig. S10 (b) and 10 (c)]. It gives strong evidence to our hypothesis that the good merging of the h-BN domains depends on the copper crystalline orientation. Similar work has been reported by Li *et al.* in which they have demonstrated seamless merging is favorable on Cu (110) while the inhomogeneous and irregular h-BN growth takes place on Cu (111)

[57]. The irregularities and non-homogeneity of the h-BN grain boundaries can also be caused by uncontrolled cooling rate of the CVD furnace. It has been reported earlier in the literature that the h-BN synthesis on nickel substrate has high crystallinity when the substrate cools down with a controlled cooling rate. Takasaki *et al.* have also demonstrated in their work that a slower cooling on Cu-Ni alloys improves the segregation of carbon and enhances the continuity of the multilayer graphene [58]. However, we conclude that the controlled cooling rate does not affect the synthesized h-BN layers when copper is used as a catalytic substrate [Fig. S11]. This finding validates that merging of the h-BN domains, homogeneity, and crystallinity does not depend on the cooling rate when copper is used as a catalytic substrate. To study further the characteristics of the OA-CVD grown h-BN, the samples were transferred on standard silicon substrates covered with a 300-nm thick silicon dioxide layer. Fig. 5(b) and 5(c) show the optical microscopy image and SEM image of non-continuous and continuous h-BN, respectively. Fig. 5(d) and 5(e) show the step height measurement by AFM at the edges of the h-BN domain. The thickness is estimated between 2 and 4 nm, which should correspond to 6–10 layers of the h-BN, however, multiple effects such as surface corrugation of the h-BN layers, that we will discuss later, presence of PMMA residues, difference in electrostatic force between the probe and the h-BN/SiO<sub>2</sub>, SiO<sub>2</sub>/h-BN gap can falsely increase the thickness of the film. This makes us believe that the actual thickness is closer to around 6 layers of h-BN when measuring the 2–4 nm. To explain the quality and uniformity of the h-BN layers, we characterized our transferred samples by Raman spectroscopy. The Raman fingerprint of the h-BN layers occurs due to the E<sub>2g</sub> in-plane vibration mode of the boron and nitrogen atoms. The Raman signature of the bulk h-BN was found around 1360–1365 cm<sup>-1</sup> that shows a blue shift in the spectrum when reduced to a few layers. We found that in our transferred h-BN samples the characteristic peak of Raman is located between 1369 and 1370 cm<sup>-1</sup> [Fig. 6(a)]. However,

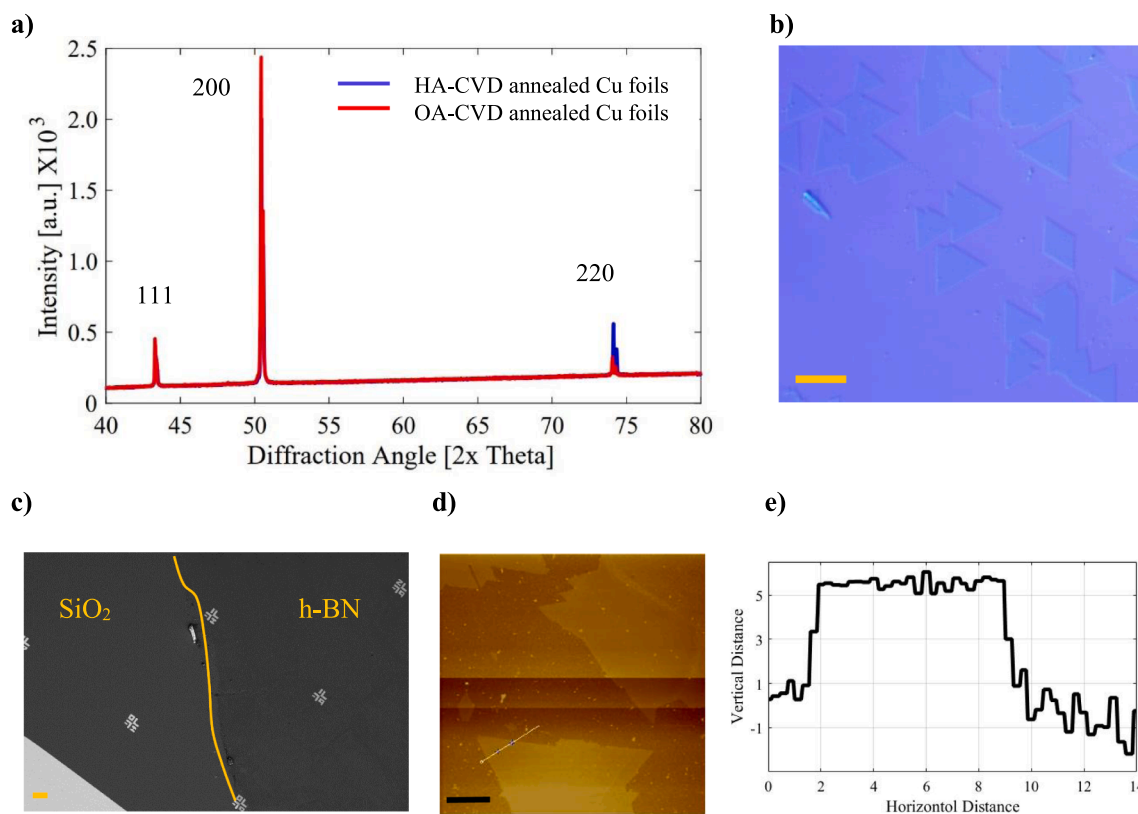


**Fig. 5.** Microscopic analysis of OA-CVD synthesized h-BN. (a) XRD patterns of HA-CVD processed and OA-CVD processed copper foils. (b) Optical microscopy images showing non-continuous triangular-shaped distinguished h-BN domains. (c) SEM image of continuous h-BN layer transferred on 300 nm SiO<sub>2</sub> surface. (d) Step height measurement of triangular h-BN domains on 300 nm silicon dioxide surface. (e) AFM height profile of h-BN flake. The scale bars for b, c, and d are 10  $\mu\text{m}$ .

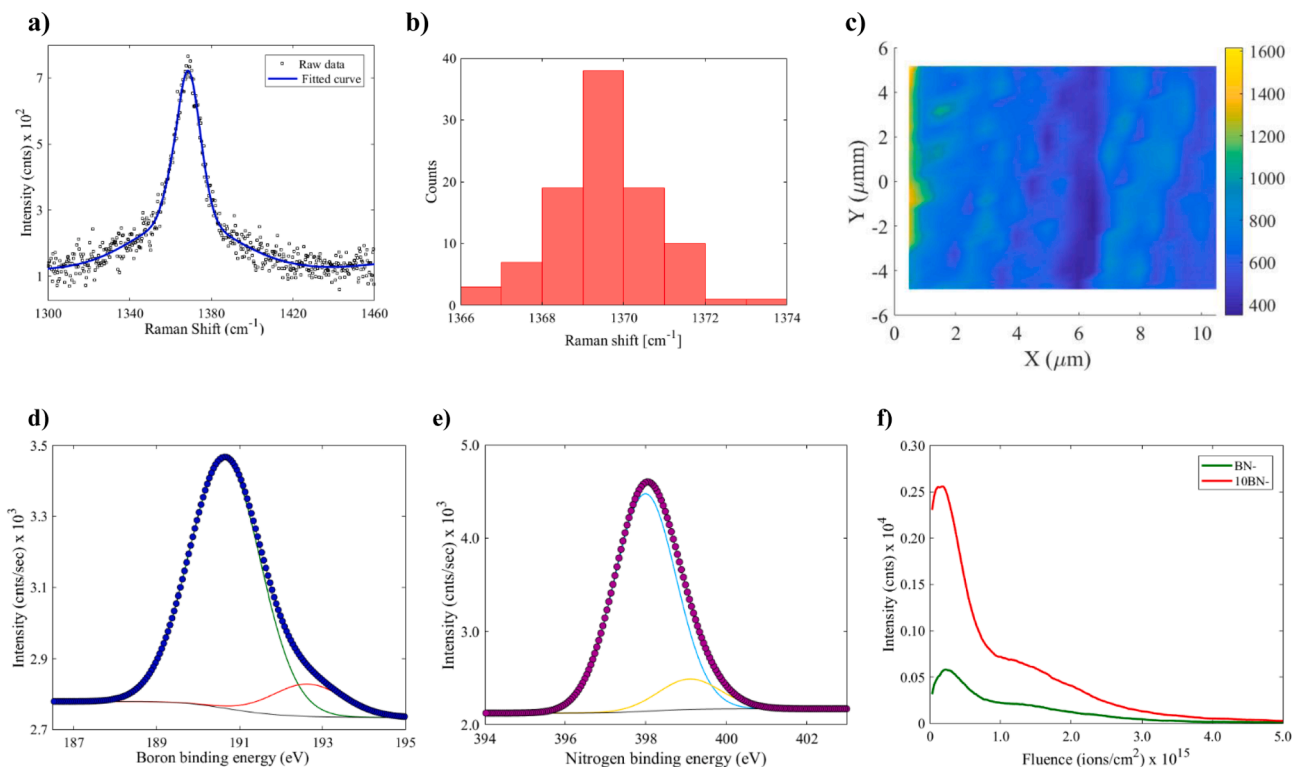


**Fig. 6.** The Quality assessment of OA-CVD synthesized h-BN. (a) Raman signature of h-BN transferred on 300 nm silicon dioxide substrate. (b–c) XPS analysis of h-BN samples on copper foils. (b) Binding energy of Boron. (c) Binding energy of nitrogen. (d) ToF-SIMS depth profile of OA-CVD synthesized h-BN layers on copper foils. (e) Absorption spectra of h-BN layers transferred on quartz slides.

our statistical analysis demonstrates the small deviation of  $\pm 3$  cm<sup>-1</sup> in the spectrum location [Fig. 6(b)] that has been carried out individually separated domains randomly as shown in Fig. 5(b). The average full width and half maxima (FWHM) of the Raman signal is 15.83 cm<sup>-1</sup> with a standard deviation of  $\pm 2.7$  cm<sup>-1</sup>. The uniformity of the h-BN layers demonstrated by the Raman intensity mapping of the characteristic peak (E<sub>2g</sub>) of h-BN. The Raman mapping is carried out on a continuous h-BN region as shown in Fig. 5(c). The Raman heat map of the h-BN characteristic peak is nearly uniform that shows a highly homogenous h-BN region on the substrate [Fig. 6(c)]. Our Raman data is quite consistent with the previously published reports [36]. Intrinsic chemical properties and atomic concentration of OA-CVD synthesized h-BN layers are characterized by XPS and ToF-SIMS spectroscopy directly on the copper foil to avoid any possible contamination caused by the transfer process. Thanks to the XPS analysis, we confirm the binding energy of boron is 190.77 eV whilst the binding energy of nitrogen is around 398.14 eV [Fig. 6(d) and 6(e)] almost similar to the values as previously reported in the literature. [25,28] A small satellite peak appears along with boron binding energy which is fitted as B<sub>2</sub>O<sub>3</sub>. On the other hand, a similar peak appeared along with nitrogen that is identified as organic nitrogen (CN). We believe that this contamination is involved after the synthesis of the sample during mild oxidation of copper substrate to visualize the h-BN domains using a microscope. On the other hand, the presence of CN species might be due to the attachment of nitrogen to residual carbon of copper substrate. Similar traces also have been observed by SIMS analysis as shown in Fig. S12 (a). SIMS depth profiling shows that h-BN formation takes place on the surface and is reduced to thickness with the increase in depth [Fig. 6(f)]. XPS's full elemental survey is illustrated in Fig. S12 (d). Moreover, the XPS analysis also confirms that the collective N: B ratio is around 1:1.01  $\pm$  0.05. A slightly higher concentration of boron is in agreement with the larger solubility of boron in the copper foil (see Table S3 and Fig. S2). The quantitative analysis carried by XPS shows that the presence of all the impurities is less than 1%. A detailed description of quantitative analysis as atomic concentration is given in

Table S3. The traces of atmospheric carbon and oxygen have also been demonstrated in Fig. S12 (a) and (b). The internal physical properties were further studied by PEEM, and  $\mu$ -ARPES spectroscopies. Similar to XPS and ToF-SIMS analysis, the PEEM and  $\mu$ -ARPES studies also have been carried out directly on the copper foils (h-BN/Cu) to avoid the charging effects when h-BN is exposed to high-energy photoelectrons. The work function (WF) maps were obtained by fitting EF-PEEM images close to the WF cut-off edge, using a pixel-by-pixel gradient extrapolation to the background. The WF maps for OA-CVD h-BN sample are shown in Fig. 7(a) and 7(b) across a 2-μm area which reveals the homogeneous layer of h-BN with an average WF of 4.79 eV, indicating the formation of metal insulator junction due to h-BN/Cu interaction. However, in the case of the HA-CVD sample, the inhomogeneity and lower WF of 4.55 eV beckons towards the lower quality of the surface of multilayer h-BN caused by smaller domain size. It demonstrates that the quality of h-BN increases with the increase in the size of domains. A comparison of WF of OA-CVD and HACVD samples is demonstrated in Fig. S13 (a–b). The full-wave vector micro angle-resolved photoemission spectroscopy ( $\mu$ -ARPES) of h-BN on Cu substrate for the OA-CVD sample at selected binding energy is shown in Fig. 7(c–f). A substantial broadening of the dispersion states in ARPES is observed which can be attributed to the surface corrugation. Fig. 7(d) and (e) reveals the band dispersion along with the M-Γ-M and K-Γ-K symmetry points of the first Brillouin zone of 2D h-BN. The reference image shows the region of interest where the ARPES was taken along with the Brillouin zone (hexagon). Overall, the  $\mu$ -ARPES analysis establishes the high quality of h-BN in OA-CVD samples. The dispersion states can be seen which indicates conservation of momentum on the surface demonstrating the enhanced and better quality of OA-CVD samples than the HA-CVD samples where no dispersion of state is observed, as can be seen in Fig. S13 (c) and (d). This validates the fact that pre-oxidized copper foils certainly increase the intrinsic functional quality of h-BN domains. The surface topography of the OA-CVD synthesized h-BN as revealed by PEEM (both with and without the contrast aperture) can be seen in Fig. 8

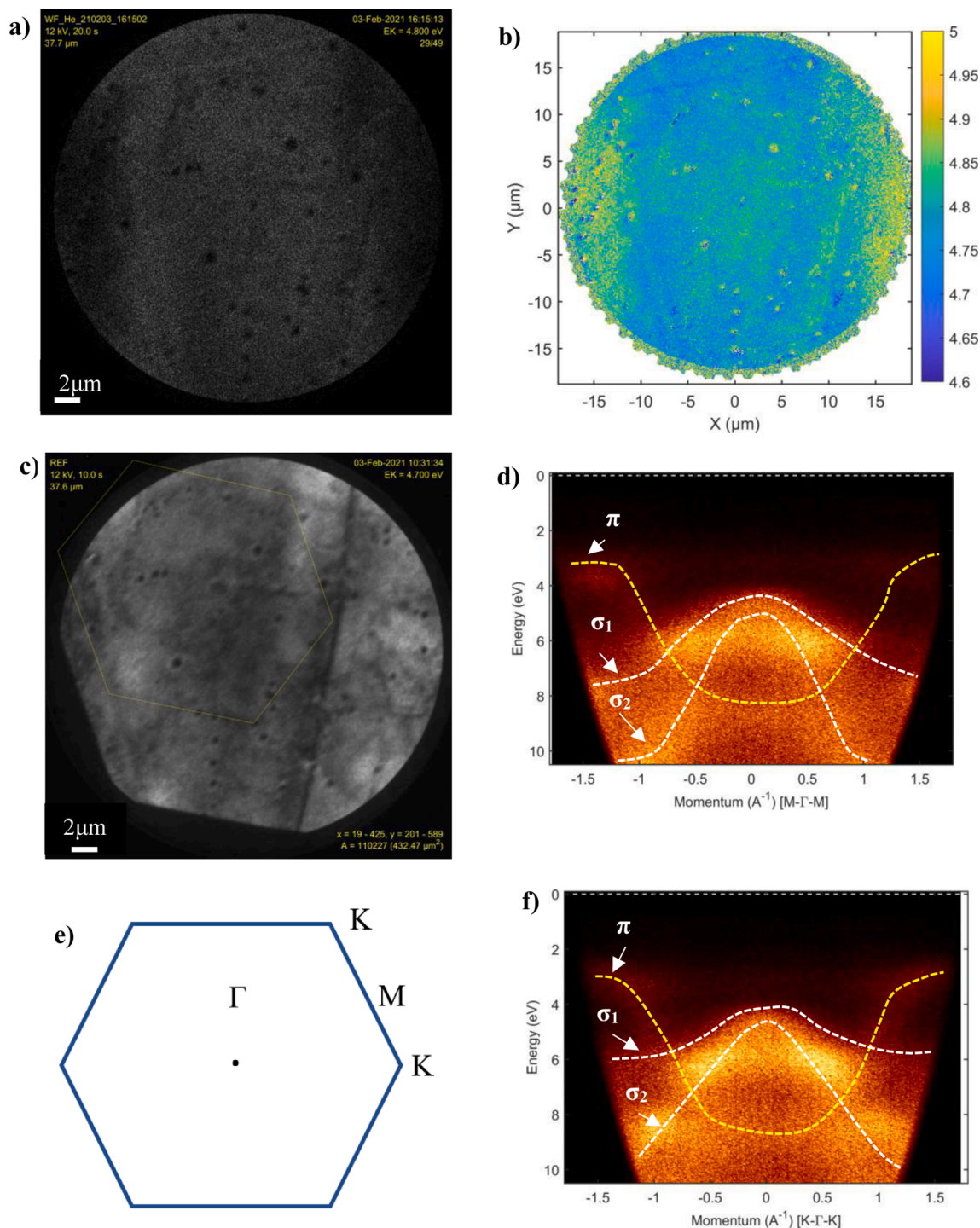


**Fig. 7.** Workfunction and ARPES measurement (a–b) PEEM analyses of h-BN layers on copper foil. (a) Reference image. With the region of interest. (b) Work function map at low temperature. (c) Reference image with the region of interest with the hexagon indicating the first Brillouin zone of h-BN. (d) ARPES spectra of OA-CVD hBN at a low temperature of 34 K, along M- $\Gamma$ -M valley with the top of the  $\sigma_1$  and  $\sigma_2$  band located at the  $\Gamma$  point and a section of the  $\pi$  band at the top edges, depicted by the white and yellow dashed lines, respectively. (e) A small hexagon represents the location of M,  $\Gamma$ , and K valleys in momentum space. (f) First Brillouin zone for h-BN layer along K- $\Gamma$ -K valley. The white and yellow dashed curves depict the dispersions of the  $\sigma$  and  $\pi$  band, respectively. The overall energy resolution of the image is 40 meV.

(a–k) which shows an important feature of surface corrugation of the h-BN layer on the surface of copper in the form of light and dark bands across the surface. The surface corrugation has been theoretically demonstrated by Mirabedini *et al.* [64] in which a 2D h-BN layer has been seen to form a buckled alignment or corrugation on the surface of the diamond substrate to relax the compressive strain imposed by the substrate geometry. A similar phenomenon has been seen to occur in the

case of graphene on Ge [65] and SiC substrates [66]. The effects of these corrugations are negligible on the electronic properties of the h-BN layer. This corrugation results in the stronger bonding of h-BN to the substrate near the locations where the curvature is large due to the distortion of orbital hybridization as the  $sp^2$  bonds bend in the rippled sheet. The domain orientation also has been observed by probing 6-fold symmetry in ARPES analyses. We have discovered there is a small

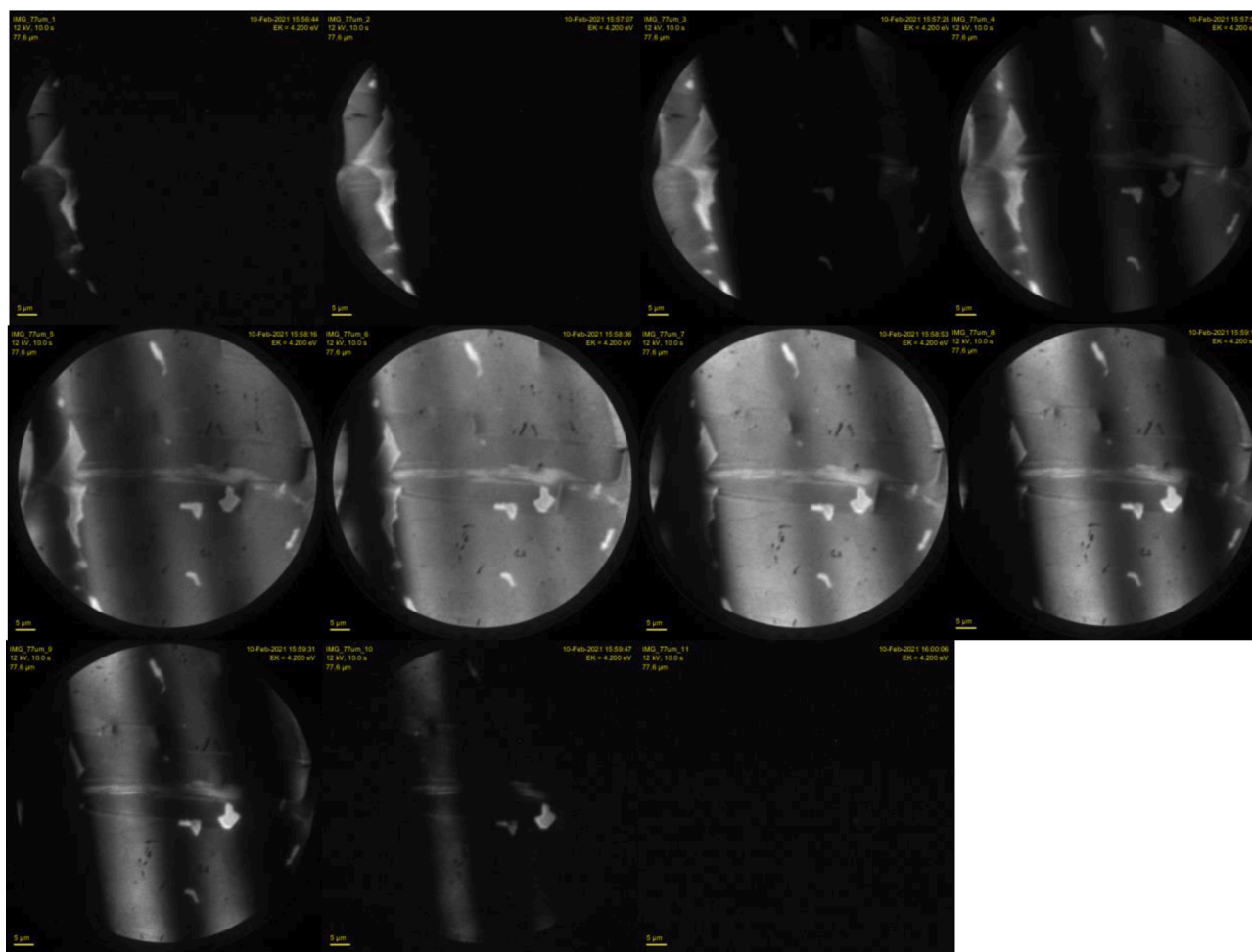


**Fig. 8.** The Quality assessment of OA-CVD synthesized h-BN. (a) Surface topography of h-BN layers demonstrated by dark and light bands.

mismatch of  $10\text{--}15^\circ$  between the domains that could be attributed to the polycrystalline nature of the copper substrate [Fig. S14].

#### 4. Conclusion

In conclusion, we have illustrated that the oxygen-activated CVD process dramatically increases the size of h-BN domains. An integrated strategy of surface confinement together with the pre-oxidized copper foil with a controlled flow of oxygen in the CVD chamber enhances the domain size from a few microns to  $\sim 180\ \mu\text{m}$ . These large area domains merge and form centimeter-sized crystals of multilayer h-BN. It is demonstrated that these large area h-BN domains do not originate due to any specific crystal orientation of the copper substrate. Further annealing in the presence of hydrogen diminishes the passive oxide layer, hence resulting in smaller h-BN domains. Raman and  $\mu$ -ARPES analysis exhibit that the synthesized h-BN is of high quality having a mean work-function of about 4.79 eV. The oxygenated inert environment produced by Ar + Ar/O<sub>2</sub> along with the surface confinement, hence pave a simple pathway to grow large-scale h-BN layers with high reproducibility.

#### CRediT authorship contribution statement

**Mohammad Wasil Malik:** Conceptualization, Data curation, Formal analysis, Investigation, Methodology, Writing – original draft, Writing – review & editing. **Sami Ullah:** Formal analysis, Data curation. **Bin Wang:** Conceptualization, Investigation, Formal analysis, Writing – review & editing. **Sahar Jaddi:** Investigation, Formal analysis, Writing –

review & editing. **Yun Zeng:** Validation, Visualization, Writing – review & editing. **Jean-Pierre Raskin:** Validation, Project administration, Supervision, Funding acquisition, Writing – review & editing.

#### Declaration of Competing Interest

The authors declare that they have no known competing financial interests or personal relationships that could have appeared to influence the work reported in this paper.

#### Data availability

Data will be made available on request.

#### Acknowledgement

We acknowledge the financial support Actions de Recherche Concertées ARC and NATURIST project granted by the Communauté Française de Belgique. Besides, we would like to gratefully acknowledge the Wallonia infrastructure for nanofabrication (WINFAB) for the equipment and experimental facilities. We are grateful to Wallonia electronics and communication measurements (WELCOME), microscopic characterization of functional and nanostructured materials (MICA), institute of condensed matter and nanoscience (IMCN), and institute of mechanics, materials, and civil engineering (IMMC) platforms for the characterization facilities. We would like to extend our acknowledgment to Mr. Pierre Eloy for his valuable advice in XPS analysis and Mr. Claude Poleunis for his advice and training of Tof-SIMS. We are thankful to Mr.

François Devred for his help in the XRD measurement and analysis. We are very grateful to Dr. Jude Laverock and Dr. Neil Fox from the University of Bristol, UK for their valuable advice on PEEM and  $\mu$ -ARPES analyses.

## Appendix A. Supplementary material

Supplementary data to this article can be found online at <https://doi.org/10.1016/j.jcrysgro.2023.127088>.

## References

- [1] K. Watanabe, T. Taniguchi, H. Kanda, Direct-bandgap properties and evidence for ultraviolet lasing of hexagonal boron nitride single crystal, *Nat. Mater.* 3 (2004) 404–409.
- [2] C.R. Dean, A.F. Young, I. Meric, C. Lee, L. Wang, S. Sorgenfrei, K. Watanabe, T. Taniguchi, P. Kim, K.L. Shepard, et al., Boron nitride substrates for high-quality graphene electronics, *Nat. Nanotech.* 5 (2010) 722–726.
- [3] G. Giovannetti, P.A. Khomyakov, G. Brocks, K.P.J. Van Den, J. Brink, Substrate-induced band gap in graphene on hexagonal boron nitride: ab initio density functional calculations, *Phys. Rev. B* 76 (7) (2007), 073103.
- [4] A. Woessner, M.B. Lundeberg, Y. Gao, A. Principi, P. Alonso-González, M. Carrega, K. Watanabe, T. Taniguchi, G. Vignale, M. Polini, et al., Highly confined low-loss plasmons in graphene–boron nitride heterostructures, *Nat. Mater.* 14 (2015) 421–425.
- [5] W. Kong, H. Li, K. Qiao, Y. Kim, K. Lee, Y. Nie, D. Lee, T. Osadchy, R.J. Molnar, D. K. Gaskill, et al., Polarity governs atomic interaction through two-dimensional materials, *Nat. Mater.* 17 (2018) 999–1004.
- [6] L. Britnell, R.V. Gorbachev, R. Jalil, B.D. Belle, F. Schedin, A. Mishchenko, T. Georgiou, M.I. Katsnelson, L. Eaves, S.V. Morozov, et al., Field-effect tunneling transistor based on vertical graphene heterostructures, *Science* 335 (6071) (2012) 947–950.
- [7] G.U. Siddiqui, M.M. Rehman, Y.J. Yang, K.H. Choi, A two-dimensional hexagonal boron nitride/polymer nanocomposite for flexible resistive switching devices, *J. Mater. Chem. C* 5 (2017) 862–871.
- [8] A. Falin, Q. Cai, E.J. Santos, D. Scullion, D. Qian, R. Zhang, Z. Yang, S. Huang, K. Watanabe, T. Taniguchi, M.R. Barnett, Mechanical properties of atomically thin boron nitride and the role of interlayer interactions, *Nat. Commun.* 8 (2017) 15815.
- [9] K. Zhang, Y. Feng, F. Wang, Z. Yang, J. Wang, Two dimensional hexagonal boron nitride (2D-hBN): synthesis, properties and applications, *J. Mater. Chem. C* 5 (46) (2017) 11992–12022.
- [10] L. Song, L. Ci, H. Lu, P.B. Sorokin, C. Jin, J. Ni, A.G. Kvashnin, D.G. Kvashnin, J. Lou, B.I. Yakobson, et al., Large scale growth and characterization of atomic hexagonal boron nitride layers, *Nano Lett.* 10 (8) (2010) 3209–3215.
- [11] S. Dai, Z. Fei, Q. Ma, A.S. Rodin, M. Wagner, A.S. McLeod, M.K. Liu, W. Gannett, W. Regan, K. Watanabe, et al., Tunable phonon polaritons in atomically thin van der Waals crystals of boron nitride, *Science* 343 (6175) (2014) 1125–1129.
- [12] S. Dai, Q. Ma, M.K. Liu, T. Andersen, Z. Fei, M.D. Goldflam, M. Wagner, K. Watanabe, T. Taniguchi, M. Thiemens, et al., Graphene on hexagonal boron nitride as a tunable hyperbolic metamaterial, *Nat. Nanotech.* 10 (2015) 682–686.
- [13] R. Ribeiro-Palau, C. Zhang, K. Watanabe, T. Taniguchi, J. Hone, C.R. Dean, Twistable electronics with dynamically rotatable heterostructures, *Science* 361 (6403) (2018) 690–693.
- [14] A.L. Exarhos, D.A. Hopper, R.N. Patel, M.W. Doherty, L.C. Bassett, Magnetic-field-dependent quantum emission in hexagonal boron nitride at room temperature, *Nat. Commun.* 10 (2019) 222.
- [15] R. Bourrellier, S. Meuret, A. Tararan, O. Stéphan, M. Kociak, L.H. Tizei, A. Zobelli, Bright UV single photon emission at point defects in h-BN, *Nano Lett.* 16 (7) (2016) 4317–4321.
- [16] T.Q. Vuong, G. Cassabois, P. Valvin, E. Rousseau, A. Summerfield, C.J. Mellor, Y. Cho, T.S. Cheng, J.D. Albar, L. Eaves, et al., Deep ultraviolet emission in hexagonal boron nitride grown by high-temperature molecular beam epitaxy, *2D Mater.* 4 (2017), 021023.
- [17] Y. Shi, C. Hamsen, X. Jiá, K.K. Kim, A. Reina, M. Hofmann, A.L. Hsu, K. Zhang, H. Li, Z.Y. Juang, M.S. Dresselhaus, Synthesis of few-layer hexagonal boron nitride thin film by chemical vapor deposition, *Nano Lett.* 10 (10) (2010) 4134–4139.
- [18] K.K. Kim, A. Hsu, X. Jia, S.M. Kim, Y. Shi, M. Hofmann, D. Nezich, J.F. Rodriguez-Nieva, M. Dresselhaus, T. Palacios, et al., Synthesis of monolayer hexagonal boron nitride on Cu foil using chemical vapor deposition, *Nano Lett.* 12 (1) (2012) 161–166.
- [19] C.M. Orofeo, S. Suzuki, H. Kageshima, H. Hibino, Growth and low-energy electron microscopy characterization of monolayer hexagonal boron nitride on epitaxial cobalt, *Nano Res.* 6 (5) (2013) 335–347.
- [20] G. Lu, T. Wu, Q. Yuan, H. Wang, H. Wang, F. Ding, X. Xie, M. Jiang, Synthesis of large single-crystal hexagonal boron nitride grains on Cu–Ni alloy, *Nat. Commun.* 6 (2015) 6160.
- [21] S. Caneva, R.S. Weatherup, B.C. Bayer, R. Blume, A. Cabrero-Vilatelá, P. Braeuninger-Weimer, M.B. Martin, R. Wang, C. Baetz, R. Schloegl, et al., Controlling catalyst bulk reservoir effects for monolayer hexagonal boron nitride CVD, *Nano Lett.* 16 (2) (2016) 1250–1261.
- [22] J.C. Koepke, J.D. Wood, Y. Chen, S.W. Schmucker, X. Liu, N.N. Chang, L. Nienhaus, J.W. Do, E.A. Carrion, J. Hewaparakrama, et al., Role of pressure in the growth of hexagonal boron nitride thin films from ammonia-borane, *Chem. Mater.* 28 (12) (2016) 4169–4179.
- [23] Y. Stehle, H.M. Meyer III, R.R. Unocic, M. Kidder, G. Polizos, P.G. Datskos, R. Jackson, S.N. Smirnov, I.V. Vlasiouk, Synthesis of hexagonal boron nitride monolayer: control of nucleation and crystal morphology, *Chem. Mater.* 27 (23) (2015) 8041–8047.
- [24] S. Caneva, R.S. Weatherup, B.C. Bayer, B. Brennan, S.J. Spencer, K. Mingard, A. Cabrero-Vilatelá, C. Baetz, A.J. Pollard, R. Hofmann, Nucleation control for large, single crystalline domains of monolayer hexagonal boron nitride via Si-doped Fe catalysts, *Nano Lett.* 15 (3) (2015) 1867–1875.
- [25] R.Y. Tay, M.H. Griep, G. Mallick, S.H. Tsang, R.S. Singh, T. Tumlin, E.H. Teo, S. P. Karna, Growth of large single-crystalline two-dimensional boron nitride hexagons on electropolished copper, *Nano Lett.* 14 (2) (2014) 839–846.
- [26] R.Y. Tay, X. Wang, S.H. Tsang, G.C. Loh, R.S. Singh, H. Li, G. Mallick, E.H. Teo, A systematic study of the atmospheric pressure growth of large-area hexagonal crystalline boron nitride film, *J. Mater. Chem. C* 2 (2014) 1650–1657.
- [27] A. Ismach, H. Chou, P. Mende, A. Dolocan, R. Addou, S. Aloni, R. Wallace, R. Feenstra, R.S. Ruoff, L. Colombo, Carbon-assisted chemical vapor deposition of hexagonal boron nitride, *2D Mater.* 4 (2017), 025117.
- [28] H. Park, T.K. Kim, S.W. Cho, H.S. Jang, S.I. Lee, S.Y. Choi, Large-scale synthesis of uniform hexagonal boron nitride films by plasma-enhanced atomic layer deposition, *Sci. Rep.* 7 (2017) 40091.
- [29] H. Jeong, D.Y. Kim, J. Kim, S. Moon, N. Han, S.H. Lee, O.F. Okello, K. Song, S. Y. Choi, J.K. Kim, Wafer-scale and selective-area growth of high-quality hexagonal boron nitride on Ni (111) by metal-organic chemical vapor deposition, *Sci. Rep.* 9 (2019) 5736.
- [30] C.L. Tsai, Y. Kobayashi, T. Akasaka, M. Kasu, Molecular beam epitaxial growth of hexagonal boron nitride on Ni (1 1 1) substrate, *J. Cryst. Growth* 311 (10) (2009) 3054–3057.
- [31] T.S. Cheng, A. Summerfield, C.J. Mellor, A. Davies, A.N. Khlobystov, L. Eaves, C. T. Foxon, P.H. Beton, S.V. Novikov, High-temperature molecular beam epitaxy of hexagonal boron nitride layers, *J. Vac. Sci. Technol. B* 36 (2018) 02D103.
- [32] J.M. Wofford, S. Nakhaie, T. Krause, X. Liu, M. Ramsteiner, M. Hanke, H. Riechert, J.M. Lopes, A hybrid MBE-based growth method for large-area synthesis of stacked hexagonal boron nitride/graphene heterostructures, *Sci. Rep.* 7 (2017) 43644.
- [33] H. Ye, T. Lu, C. Xu, B. Han, N. Meng, L. Xu, Liquid-phase exfoliation of hexagonal boron nitride into boron nitride nanosheets in common organic solvents with hyperbranched polyethylene as stabilizer, *Macromol. Chem. Phys.* 219 (2018) 1700482.
- [34] B. Zhang, Q. Wu, H. Yu, C. Bulin, H. Sun, R. Li, X. Ge, R. Xing, High-efficient liquid exfoliation of boron nitride nanosheets using aqueous solution of alkanolamine, *Nanoscale Res. Lett.* 12 (2017) 596.
- [35] W. Cao, J. Wang, M. Ma, Exfoliation of two-dimensional materials: the role of entropy, *J. Phys. Chem. Lett.* 10 (5) (2019) 981–986.
- [36] R.J. Chang, X. Wang, S. Wang, Y. Sheng, B. Porter, H. Bhaskaran, J.H. Warner, Growth of large single-crystalline monolayer hexagonal boron nitride by oxide-assisted chemical vapor deposition, *Chem. Mater.* 29 (15) (2017) 6252–6260.
- [37] R. Han, M.H. Khan, A. Angeloski, G. Casillas, C.W. Yoon, X. Sun, Z. Huang, Hexagonal boron nitride nanosheets grown via chemical vapor deposition for silver protection, *ACS Appl. Nano Mater.* 2 (5) (2019) 2830–2835.
- [38] J.S. Lee, S.H. Choi, S.J. Yun, Y.I. Kim, S. Boandoh, J.H. Park, B.G. Shin, H. Ko, S. H. Lee, Y.M. Kim, et al., Wafer-scale single-crystal hexagonal boron nitride film via self-collimated grain formation, *Science* 362 (6416) (2018) 817–821.
- [39] M. Corso, W. Auwärter, M. Muntwiler, A. Tamai, T. Greber, J. Osterwalder, Boron nitride nanomesh, *Science* 303 (5655) (2004) 217–220.
- [40] H. Cun, A. Hemmi, E. Miniussi, C. Bernard, B. Probst, K. Liu, D.T. Alexander, A. Kleibert, G. Mette, M. Weinel, et al., Centimeter-sized single-orientation monolayer hexagonal boron nitride with or without nanovoids, *Nano Lett.* 18 (2) (2018) 1205–1212.
- [41] T.A. Chen, C.P. Chuu, C.C. Tseng, C.K. Wen, H.S. Wong, S. Pan, R. Li, T.A. Chao, W. C. Chueh, Y. Zhang, et al., Wafer-scale single-crystal hexagonal boron nitride monolayers on Cu (111), *Nature* 579 (2020) 219–223.
- [42] L. Wang, B. Wu, H. Liu, L. Huang, Y. Li, W. Guo, X. Chen, P. Peng, L. Fu, Y. Yang, et al., Water-assisted growth of large-sized single crystal hexagonal boron nitride grains, *Mater. Chem. Front.* 1 (2017) 1836–1840.
- [43] G. Kim, A.R. Jang, H.Y. Jeong, Z. Lee, D.J. Kang, H.S. Shin, Growth of high-crystalline, single-layer hexagonal boron nitride on recyclable platinum foil, *Nano Lett.* 13 (4) (2013) 1834–1839.
- [44] J. Yin, J. Yu, X. Li, J. Li, J. Zhou, Z. Zhang, W. Guo, Large single-crystal hexagonal boron nitride monolayer domains with controlled morphology and straight merging boundaries, *Small* 11 (35) (2015) 4497–4502.
- [45] A. Ismach, H. Chou, D.A. Ferrer, Y. Wu, S. McDonnell, H.C. Floresca, A. Covacevich, C. Pope, R. Piner, M.J. Kim, et al., Toward the controlled synthesis of hexagonal boron nitride films, *ACS Nano* 6 (7) (2012) 6378–6385.
- [46] Y. Cheng, X. Yin, Y. Liu, S. Li, L. Cheng, L. Zhang, BN coatings prepared by low pressure chemical vapor deposition using boron trichloride–ammonia–hydrogen–argon mixture gases, *Surf. Coat. Technol.* 204 (2010) 2797–2802.
- [47] L. Qin, J. Yu, M. Li, F. Liu, X. Bai, Catalyst-free growth of mono- and few-atomic-layer boron nitride sheets by chemical vapor deposition, *Nanotechnology* 22 (2011), 215602.
- [48] W. Auwärter, H.U. Suter, H. Sachdev, T. Greber, Synthesis of one monolayer of hexagonal boron nitride on Ni (111) from B-trichloroborazine (CIBNH)<sub>3</sub>, *Chem. Mater.* 16 (2) (2004) 343–345.

- [49] R.Y. Tay, H. Li, S.H. Tsang, M. Zhu, M. Loeblein, L. Jing, F.N. Leong, E.H. Teo, Trimethylamine borane: a new single-source precursor for monolayer h-BN single crystals and h-BCN thin films, *Chem. Mater.* 28 (7) (2016) 2180–2190.
- [50] V. Babenko, G. Lane, A.A. Koos, A.T. Murdock, K. So, J. Britton, S.S. Meysami, J. Moffat, N. Grobert, Time dependent decomposition of ammonia borane for the controlled production of 2D hexagonal boron nitride, *Sci. Rep.* 7 (2017) 14297.
- [51] W. Lin, P. Zhuang, D. Akinwande, X.A. Zhang, W. Cai, Oxygen-assisted synthesis of hBN films for resistive random access memories, *Appl. Phys. Lett.* 115 (2019), 073101.
- [52] J. Yin, X. Liu, W. Lu, J. Li, Y. Cao, Y. Li, Y. Xu, X. Li, J. Zhou, C. Jin, et al., Aligned growth of hexagonal boron nitride monolayer on germanium, *Small* 11 (40) (2015) 5375–5380.
- [53] J. Li, Y. Li, J. Yin, X. Ren, X. Liu, C. Jin, W. Guo, Growth of polar hexagonal boron nitride monolayer on nonpolar copper with unique orientation, *Small* 12 (27) (2016) 3645–3650.
- [54] X. Li, Y. Li, Q. Wang, J. Yin, J. Li, J. Yu, W. Guo, Oxygen-suppressed selective growth of monolayer hexagonal boron nitride on copper twin crystals, *Nano Res.* 10 (3) (2017) 826–833.
- [55] M. Bowden, T. Autrey, I. Brown, M. Ryan, The thermal decomposition of ammonia borane: a potential hydrogen storage material, *Curr. Appl. Phys.* 8 (2008) 498–500.
- [56] M. Wu, Z. Zhang, X. Xu, Z. Zhang, Y. Duan, J. Dong, R. Qiao, S. You, L. Wang, J. Qi, et al., Seeded growth of large single-crystal copper foils with high-index facets, *Nature* 581 (2020) 406–410.
- [57] L. Wang, X. Xu, L. Zhang, R. Qiao, M. Wu, Z. Wang, S. Zhang, J. Liang, Z. Zhang, Z. Zhang, et al., Epitaxial growth of a 100-square-centimetre single-crystal hexagonal boron nitride monolayer on copper, *Nature* 570 (2019) 91–95.
- [58] Y. Takesaki, K. Kawahara, H. Hibino, S. Okada, M. Tsuji, H. Ago, Highly uniform bilayer graphene on epitaxial Cu–Ni (111) alloy, *Chem. Mater.* 28 (13) (2016) 4583–4592.
- [59] Q. Wu, J.H. Park, S. Park, S.J. Jung, H. Suh, N. Park, W. Wongwiriyan, S. Lee, Y. H. Lee, Y.-J. Song, Single crystalline film of hexagonal boron nitride atomic monolayer by controlling nucleation seeds and domains, *Sci. Rep.* 5 (2015) 16159.
- [60] H. Zhou, W.-J. Yu, L. Liu, R. Cheng, Y. Chen, X. Huang, Y. Liu, Y. Wang, Y. Huang, X. Duan, Chemical vapour deposition growth of large single crystals of monolayer and bilayer graphene, *Nat. Commun.* 4 (2013) 2096.
- [61] Y. Hao, L. Wang, Y. Liu, H. Chen, X. Wang, C. Tan, S. Nie, J.W. Suk, T. Jiang, T. Liang, et al., Oxygen-activated growth and bandgap tunability of large single-crystal bilayer graphene, *Nat. Nanotech.* 11 (2016) 426–431.
- [62] L. Britnell, R.V. Gorbachev, R. Jalil, B.D. Belle, F. Schedin, M.I. Katsnelson, L. Eaves, S.V. Morozov, A.S. Mayorov, N.M. Peres, et al., Electron tunneling through ultrathin boron nitride crystalline barriers, *Nano Lett.* 12 (3) (2012) 1707–1710.
- [63] V. Babenko, Y. Fan, V.P. Veigang-Radulescu, B. Brennan, A.J. Pollard, O. Burton, J. A. Alexander-Webber, R.S. Weatherup, B. Canto, M. Otto, et al., Oxidising and carburising catalyst conditioning for the controlled growth and transfer of large crystal monolayer hexagonal boron nitride, *2D Mater.* 7 (2020), 024005.
- [64] P.S. Mirabedini, B. Debnath, M.R. Neupane, P. Alex Greaney, A. Glen Birdwell, D. Ruzmetov, K.G. Crawford, P. Shah, J. Weil, T.G. Ivanov, Structural and electronic properties of 2D (graphene, hBN)/H-terminated diamond (100) heterostructures, *Appl. Phys. Lett.* 117 (2020), 121901.
- [65] P.C. Rogge, M.E. Foster, J.M. Wofford, K.F. McCarty, N.C. Bartelt, O.D. Dubon, On the rotational alignment of graphene domains grown on Ge (110) and Ge (111), *MRS Commun.* 5 (3) (2015) 539–546.
- [66] X. Tang, S. Xu, X. Wang, Corrugated epitaxial graphene/SiC interfaces: photon excitation and probing, *Nanoscale* 6 (2014) 8822–8830.
- [67] S. Sharma, K. Sharma, M.S. Rosmi, Y. Yaakob, M.I. Araby, H. Ohtani, G. Kalita, M. Tanemura, Morphology-controlled synthesis of hexagonal boron nitride crystals by chemical vapor deposition, *Cryst. Growth Des.* 16 (11) (2016) 6440–6445.
- [68] Y. Song, D. Pan, Y. Cheng, P. Wang, P. Zhao, H. Wang, Growth of large graphene single crystal inside a restricted chamber by chemical vapor deposition, *Carbon* 95 (2015) 1027–1032.
- [69] C. Wang, W. Chen, C. Han, G. Wang, B. Tang, C. Tang, Y. Wang, W. Zou, W. Chen, X.-A. Zhang, S. Qin, S. Chang, L. Wang, Growth of millimeter-size single crystal graphene on Cu foils by circumfluence chemical vapor deposition, *Sci. Rep.* 4 (2014) 1–5.
- [70] C.-C. Chen, C.-J. Kuo, C.-D. Liao, C.-F. Chang, C.-A. Tseng, C.-R. Liu, Y.-T. Chen, Growth of large-area graphene single crystals in confined reaction space with diffusion-driven chemical vapor deposition, *Chem. Mater.* 27 (2015) 6249–6258.
- [71] J.R. Davis, *Copper and Copper Alloys*. ASM Specialty, Handbook, ASM International, 2001.
- [72] B. Huet, J.-P. Raskin, Pressure-controlled chemical vapor deposition of single-layer graphene with millimeter-size domains on thin Cu film, *Chem. Mater.* 29 (8) (2017) 3431–3440.
- [73] J. Li, D. Wang, L.-J. Wan, Unexpected functions of oxygen in a chemical vapor deposition atmosphere to regulate graphene growth modes, *Chem. Commun.* 51 (2015) 15486–15489.
- [74] B. Huet, J.-P. Raskin, Role of Cu in-situ annealing in controlling the chemical vapor deposition of millimeter-size graphene domains, *Carbon* 129 (April 2018) 270–280.